Analytical and Bioanalytical Chemistry (2021) 413:3177–3191
https://doi.org/10.1007/s00216-021-03255-1

RESEARCH PAPER

Fabrication of target specific solid-state optical sensors using chromoionophoric probe–integrated porous monolithic polymer and silica templates for cobalt ions

Naveen Kumar Sompalli[1] · Prabhakaran Deivasigamani[1]

Received: 5 December 2020 / Revised: 23 February 2021 / Accepted: 26 February 2021 / Published online: 6 March 2021

Abstract

The article demonstrates the design of two solid-state sensors for the capturing of industrially relevant ultra-trace Co(II) ions using porous monolithic silica and polymer templates. The mesoporous silica reveals high surface area and voluminous pore dimensions that ensures homogeneous anchoring of 4-((5-(allylthio)-1,3,4-thiadiazol-2-yl)diazenyl)benzene-1,3-diol, as the chromoionophore. We report a first of its kind solid-state macro-/meso-porous polymer monolithic optical sensor from a monomeric chromoionophore, i.e., 2-(4-butylphenyl)diazenyl)-2-hydroxybenzylidene)hydrazine-1-carbothioamide. The monolithic solid-state sensors are characterized using HR-TEM-SAED, FE-SEM-EDAX, p-XRD, XPS, $^{29}Si/^{13}C$ CPMAS NMR, FT-IR, TGA, and BET/BJH analysis. The electron microscopic images reveal a highly ordered hexagonal mesoporous network of honeycomb pattern for silica monolith, and a long-range macroporous framework with mesoporous channels for polymer monolith. The sensors offer exclusive ion-selectivity and sensitivity for trace cobalt ions, through a concentration proportionate visual color transition, with a response kinetics of ≤ 5 min. The optimization of ion-sensing performance reveals an excellent detection limit of 0.29 and 0.15 ppb for Co(II), using silica- and polymer-based monolithic sensors, respectively. The proposed sensors are tested with industrial wastewater and spent Li-ion batteries, which reveals a superior cobalt ion capturing efficiency of ≥ 99.2% (RSD: ≤ 2.07%).

Keywords Porous materials · Silica · Polymer · Optical · Cobalt sensor

Introduction

In the past few decades, the anthropogenic release of heavy metal ions (HMIs) into water resources through industrial activities has been a global issue, owing to their non-biodegradable nature [1]. There are several reports relating to the health and environmental impacts of HMIs, while exceeding their permissible limit [2]. Hence, it is of tantamount importance for their early detection, despite their potential utility in various applications [3]. In this line, cobalt is one of the widely employed HMIs in electronics, batteries, healthcare, catalysis, pigments, coloring, superalloys, etc., owing to its distinctive physicochemical properties [4]. It is noticed that cobalt compounds beyond their permissible levels can induce serious health issues ranging from vomiting, diarrhea, erratic blood pressure, lung malfunction, thyroidal disruption, cardiovascular, and neurological dysfunctions [5, 6]. Considering the toxicological nature of cobalt ions, there are numerous instrumentation techniques that are currently available for the rapid detection and determination [7]. However, these techniques are associated with severe drawbacks in terms of, necessity for skilled technicians, high operational cost, and sophisticated infrastructure. In addition, some of the analytical methods and instrumentations are associated with complications in the form of matrix interferences that compromises the selectivity and sensitivity factor. Moreover, procuring high-tech instruments remains a distant dream for most of the under-developed and developing nations to have it across their national testing laboratories, for routine analysis [8].

Over the past years, chemical sensors using supramolecules are reported for Co(II) detection, with a majority of the literature reports related to organic solvent–mediated colorimetric ion-sensing [9–11]. In this aspect, Kang et al. reported an in situ colorimetric detection method,

✉ Prabhakaran Deivasigamani
prabhakaran.d@vit.ac.in; prabhakarswordy@gmail.com

[1] Department of Chemistry, School of Advanced Sciences, Vellore Institute of Technology (VIT), Vellore, Tamil Nadu 632014, India

using an expensive Chrysoidine G dye that shows color transition from yellow to light orange for Co(II) ions, with a limit of detection (LOD) value of 100 ppb and 2000 ppb through spectrophotometric and naked-eye detection, respectively. Similarly, Na et al. developed a cobalt ion responsive chemosensor using 2-(N-(2-hydroxybenzyl)-N-((pyridin-2-yl)methyl)amino)-N-(2-hydroxyphenyl)acetamide that exhibits a ligand to metal charge transfer colorimetric response from color less to pale violet, through the oxidation of Co(II) to Co(III), with a LOD value of 107 ppb [12]. In this line, Devika et al. have developed a coumarin-based probe for the colorimetric detection of Co(II), with a color change from light yellow to yellowish red via intramolecular charge transfer mechanism, with a LOD value of 413 ppb [13]. Similarly, Liu et al. also proposed a Schiff base moiety–based coumarin derivative for Co(II) ion detection, with a LOD value of 18 ppb [14]. However, the abovementioned chemosensory systems are tolerant to foreign ions only up to fivefold concentrations, beyond which significant inferences are observed, thereby compromising the ion-selectivity and sensitivity. Moreover, the use of organic solvent–based chemosensors result in non-compatible issues for real-time analysis, apart from the generation of secondary organic pollutants. Hence, these sensory systems are not suitable for continuous monitoring due to their functional behavior pertaining only for single shot assays [15]. Hence, it is of significant importance to strategically develop simple, benign, and rapid sensing methodologies that are feasible for practical conditions, without compromising the selectivity and sensitivity features [16, 17].

In recent years, the use of nanoparticles (NPs) has gained considerable interest for the sensing of toxic analytes from various environmental sources [18]. In this aspect, Yao et al. designed a triazole-carboxyl bifunctionalized Ag NPs for the colorimetric recognition of Co(II) via self-aggregation of Ag NPs through metal-ligand interaction, with a LOD value of 414 ppb. However, these triazole-carboxyl bifunctionalized Ag NPs solution are stable only up to 10 days, thereby questioning their long-term durability and stability [19]. Similarly, Karami et al. deployed glycyrrhizic acid modified Au NPs for the selective detection of Co(II) ions with a color transition from red to blue. However, with increasing solution temperature to >50 °C, the bare Au NP solution resulted in a color change from red to blue due to the increase in the size of NPs [20]. Moreover, these NP-based sensor systems are related to recovery complications related to their small particle size of the particles and also requires tuning of shape and size of these NPs [21]. In addition, the investigation of the physicochemical properties of these NPs reveal the possibility of inducing unwanted interaction with different cellular processes that are likely to cause severe health issues in human biological system [22]. Hence, the application of NPs as chemosensors is a matter of concern owing to their high cost factor, non-recoverability/non-reusability and nanotoxicity [23]. Hence, for the fabrication of a solid-state sensory system, the structural and surface morphology of solid template, the ion-sensing probe and the adapted methodology (functionalization/immobilization) methodologies, are imperative [24]. Moreover, it is likely that such solid-state designs are likely to minimize or even eliminate the use of organic solvents, besides can serves as an alternate for classical instrumental methods during continuous monitoring.

Recently, porous monolithic materials are gaining prominence in the field of optical sensors, owing to their structural and surface properties [25, 26]. Moreover, monolithic materials are associated with continuous porous network and translucent optical properties thus serving as an excellent candidate for solid-state colorimetric sensing. Besides, these porous materials carry unique properties such as greater porosity, extraordinary adsorption capacity, tailor-made shape, geometry and morphology. These features enable distinct advantages during fabrication of solid-state optical sensors in terms of response time, better selectivity and sensitivity properties. In this line, El-Safty et al. reported the use of hexagonal mesophase- and cubic mesophase-based silica monolith materials that are modified with various colorimetric responsive ionophoric receptors for Co(II) ion recognition. These solid-state sensors allowed selective naked-eye detection of ultra-trace concentrations of Co(II) ions, and are also ion-reversible and reusable [27, 28]. Considering the prospects of silica monoliths as probe template in ion sensing, Ahmad et al. and Awual et al. have reported Co(II) ion sensors by immobilizing the Schiff base ligands into the silica sorbent [29, 30]. However, there still remains a lot of scope in the utility of mesoporous silica monolith (MSM) materials in ion-sensing applications through structural refinements, along with the possibility of exploring new class of porous monolithic materials. In this line, macroporous polymer monoliths (MPM) have gained prominence in the field of separation science, for chromatographic applications [31, 32]. However, there are hardly any literature reports on their application as solid-state optical ion-sensors, particularly, for the sensing/capturing of cobalt ions, considering their growing industrial applications.

In this article, we proffer two solid-state optical chemosensors using a (i) hexagonal design of mesoporous honeycomb array silica monolith template and (ii) macro-/meso-porous interconnected organic polymer monolithic network structure. The monoliths are tuned as solid-state colorimetric sensors through organized assembly of custom-made chromoionophoric molecules that are integrated (functionalization/impregnation) to the monolith framework. In this work, two amphiphilic chromoionophoric probes, namely 4-((5-(allylthio)-1,3,4-thiadiazol-2-yl)diazenyl)benzene-

1,3-diol (**ATDBD**), and 2-(4-butylphenyl)diazenyl)-2-hydroxybenzylidene)hydrazine-1-carbothioamide (**BDHCA**) are anchored to the monolithic silica and polymer, respectively. The solid-state sensors exhibit exceptional selectivity and sensitivity in detecting ultra-trace concentrations of Co(II) ions, through concentration proportionate visual color transitions that are recognizable through naked-eye. The sensors are capable of capturing Co(II) ions from industrial and environmental samples within a short span of time, besides outlining astounding durability and reusability features.

Experimental section

Chemicals and instrumentations

For synthesis of polymer monoliths, chemicals like ethylene glycol dimethacrylate (EGDMA, ≥98%), azobisisobutyronitrile (AIBN), and 2-vinyl pyridine (2-VP, ≥ 95%), are purchased from TCI chemicals. For mesoporous silica monolith synthesis, chemicals like tetraethylorthosilicate (TEOS, ≥ 98%), Pluronic F127, and n-dodecane (≥ 99%) are purchased from Sigma-Aldrich. The chromoionophoric probes (BDHCA and ATDBD) are synthesized using chemicals like 4-butylaniline (97%), salicylaldehyde (99%), thiosemicarbazide (99%), 2-amino-5-mercapto-1,3,4-thiadazole (98%), allyl bromide (99%), and resorcinol (99%) that are from Alfa Aesar chemicals.

The low-/wide-angle XRD pattern for monolithic optical sensors are characterized using a p-X-ray diffractometer (Bruker, D8 Advance). The surface and porosity properties of monoliths are calculated using nitrogen adsorption/desorption isotherm (Quantachrome, Autosorb-iQ). The monolith structural and surface morphologies are studied using FE-SEM-EDAX (Hitachi, S-4800), and HR-TEM-SAED (Tecnai, G2 20 S-Twin). The monolith and probe structural features are characterized by a FT-IR spectrophotometer (ThermoScientific, Nicolet iS10). The structural features of chromoionophoric ligands and monolithic templates are confirmed by $^{1}H/^{13}C$ NMR and $^{29}Si/^{13}C$ CPMAS solid-state NMR (Bruker, Avance 400 MHz), CHNS analyzer (Vario, MICRO Select EL), and an HR-ESI-MS (Waters, QToF Xevo G2-XS). The thermal stability of sensor materials is monitored by TGA (Seiko, SII 7200). The sensor elemental oxidation states are studied using an X-ray photoelectron spectroscopy (XPS, PHI 5000 VersaProb-II). The optical spectra of solid-state sensors are analyzed by using a UV-Vis-DRS (Jasco, V670) instrument. The elemental composition of environmental and synthetic samples is analyzed using an inductively coupled plasma mass spectrometer (ICP-MS, ELAN DRC-e PerkinElmer).

Synthesis of chromoionophoric probes (BDHCA and ATDBD)

For the synthesis of BDHCA probe molecules, 10 mmol of 4-butylaniline is diazotized, in the presence of $NaNO_2$ and 6 M HCl at 0 °C, and coupled with an equimolar ratio of salicylaldehyde in 10% NaOH solution to afford compound 1(a), as shown in the Supplementary Information (ESM, Section I; Scheme S1a). The resulting compound is further subjected to the condensation reaction with an equivalent amount of thiosemicarbazide dissolved in ethanol to yield the desired BDHCA ligand, a pale yellow solid. The resulting probe (of 97% yield) is purified by recrystallization with hot ethanol.

^{1}H NMR (400 MHz, DMSO), δ: 11.48 (s, 1H), 10.75 (s, 1H), 8.5 (s, 1H), 8.4 (s, 1H), 8.1 (d, 2H), 7.77 (d,3H), 7.38 (d, 2H), 7.04(d, 1H),2.68–2.34 (t, J = 8.8 Hz, 2H),1.63–1.56 (m, 2H), 1.37–1.28 (m, 2H), and 0.93–0.89 (t, J = 8.4 Hz, 3H). ***^{13}C NMR (400 MHz, DMSO) δ:*** 178.3, 159.6, 150.7, 146.0, 145.8, 139.0, 129.6(2C), 124.4, 123.3, 122.7(2C), 121.5, 117.2, 35.1, 33.3, 22.2, and 14.2. ***IR frequencies:*** O-H (3429 cm^{-1}), -NH_2- (3238 cm^{-1}), N-H (3151 cm^{-1}), C=S (1010 cm^{-1}), C=NH (1597 cm^{-1}), and N=N (1508 cm^{-1}). ***CHNS analysis:*** %C 60.79 (60.82), %H 5.84 (5.96), %N 19.53 (19.70), and %S: 8.98 (9.02). The theoretical values are denoted in parenthesis. ***HR-ESI-MS:*** 355.15.

The ATDBD probe is synthesized by the allylation of 2-amino-5-mercapto-1,3,4-thiadazole with equimolar allyl bromide in the presence of K_2CO_3, in dry acetone, at room temperature for 24 h. The **compound 2a** is subjected to diazotization and coupled with resorcinol in 10% NaOH under ice-cold condition, thus resulting in the desired orange-colored product (ATDBD, Yield 92%), as shown in the schematic representation (ESM, Section I; Scheme S1b). The product is purified by column chromatography, using (30:70) ethyl acetate-n-hexane.

^{1}H NMR (400 MHz, DMSO) δ: 11.04 (s, 2H), 7.8–7.66 (t, J = 7.66 Hz, 1H), 6.47–6.45 (m, 2H), 6.04–5.94 (m, 1H), 5.35 (d, J = 7.2 Hz, 1H), and 5.23 (d, J = 7.3 Hz, 1H). ***^{13}C NMR (400 MHz, DMSO) δ:*** 180, 167.10, 166.13, 160.56, 134.23, 132.87, 122.91, 120.06, 110.9, and 103.6. ***IR frequencies:*** O-H (3057 cm^{-1}), C-H (2045–2798 cm^{-1}), and N=N (1522 cm^{-1}). ***CHNS analysis:*** %C 44.91 (44.89), %H 3.48 (3.42), %N 19.13 (19.03), and %S: 21.62 (21.78). The theoretical values are denoted in the parenthesis. ***HR-ESI-MS:*** 294.02.

Fabrication of BDHCA impregnated MSM sensor

The 2D-hexagonal array of mesoporous honeycomb-structured MSM is prepared by a triblock copolymer surfactant mediated micro-emulsion technique–based sol-gel process, using F127 and n-dodecane, as a structure-directing

entity (SDE) and porogens, respectively [33]. The amphiphilic probe (BDHCA) is directly impregnated to the synthesized MSM template, by physical adsorption, for which a known quantity (mmol) of BDHCA ligand in 500 cm^3 of ethanol is continuously homogenized with a 1.0 g of MSM. The probe impregnation on the monolithic template is carried out through the gradual removal of solvent molecules using a rota-evaporator. The probe anchored MSM with a maximum signal response is denoted as **Sensor-I**. The sensor material is washed with deionized water to ensure the non-leachability of probe molecules and then subjected to vacuum drying for 10 h, at 40 °C. The extent of probe molecule loading onto the monolith material has been studied, which reveals a saturation limit of 0.56 mmol of BDHCA probe loading per gram of MSM, as discussed in the ESM (Section II; Table S1). However, for the effective sensing of Co(II) ions (from sub-ppb to ppb) in terms of naked-eye and spectral analysis, 0.196 mmol of BDHCA probe-coated MSM template provided the best sensing performance, particularly for the reliable monitoring of ultra-trace Co(II) ions.

Fabrication of ATDBD functionalized MPM sensor

The ATDBD functionalized MPM sensor is synthesized through one-pot bulk polymerization of ATDBD (0.5–3.0 mmol; monomer), EGDMA (10.0 mmol; cross-linker), and AIBN (1.0 wt.%; radical initiator) that are dissolved in 7.5 cm^3 of dry DMSO (porogen). The polymerization is performed in a dry Schlenk tube, and the reactant solution mixture is subjected to ultrasonic degassing, and then purged with N_2 gas for 10 min. For completion of the polymerization process, the mixture is stirred at 60 °C for 48 h. The excess monomer and the formed oligomers are removed using hexane. The resulting ATDBD functionalized MPM sensor, henceforth denoted as **Sensor-II**, is vacuum dried at 40 °C for 10 h. The polymerization reaction pertaining to the formation of Sensor-II has been included in the ESM (Section III; Fig. S1).

Analytical operation for Co(II) optical sensing

To facilitate solid-state colorimetric detection, a definite concentration of Co(II) solution are prepared in various solution pH conditions, where pH 7–8 provided the best ion-sensing performance. The various concentrations of Co(II) solution is equilibrated in a mechanical shaker with a certain quantity (4~6 mg) of sensor materials, for a specific duration (1–10 min) in a solution temperature (25–40 °C), in an overall volume of 20 cm^3. A blank (without a metal ion) is prepared in a similar procedure for color comparison during naked-eye recognition by filtering the sensor material using a membrane filter (Millipore, 25 mm cellulose nitrate). The spectral pattern resulting from charge transfer color transition due to probe-Co(II) complexation is studied using UV-Vis-DRS measurement (RSD < 2.82%, triplicate analysis). The stoichiometric ratio of Co(II)-probe (BDHCA andATDBD) complexation has been studied by Job's plot (Section IV; Fig. S2), and also confirmed by ^{1}H NMR titration (Section V; Fig. S3), as discussed in the ESM.

Collection of water samples and scrap Li-ion batteries for Co(II) sensing

The groundwater and lake water samples are collected from Industrial Area, Ranipet district, Tamil Nadu, India. A certified pre-treated electronics industry wastewater is obtained from special economic zone (SEZ), Kanchipuram district, Tamil Nadu, India. The obtained samples are spiked with known quantities of Co(II) ions and are subjecting to ICP-MS analysis to authenticate cobalt ion concentration, amidst various matrix constituents. For the sensing/recovery of cobalt ions from scarp Li-ion batteries, the active ingredients (powder) from the anode and cathode materials of Li-ion batteries are obtained from an e-waste recovery unit in Bengaluru, Karnataka, India. The sample powder (1 g) is dissolved in 25 mL of aqua regia (HNO_3:HCl, 1:3) and the homogenous solution is diluted with 975 mL of deionized water. From the resulting stock solution, 100 μL of aliquot (after dilution to 1000 mL) is pH adjusted and subjected to cobalt ion sensing using the proposed sensors. The reliability of the obtained data has been confirmed by ICP-MS analysis.

Results and discussion

Structure and surface morphology characterization of monolithic sensors

The wide-angle p-XRD pattern for MSM template, Sensor-I, and Sensor-II that reveals a consistent presence of a single and broad diffraction peak pattern, thereby confirming their amorphous characters, with peak (2θ) at 23° for both bare MSM and Sensor-I, respectively, as shown in the ESM (Section VI; Fig. S4a). In the case of MPM-based Sensor-II, a broad continuous peak with a peak maxima (2θ) at 28° is observed (ESM, Section VI; Fig. S4b). The comparison between bare MSM and Sensor-I reveals a slight shift in the diffraction peaks and a decline in the peak intensity, for Sensor-I, without altering its amorphous nature. This pattern confirms the dispersion/immobilization of BDHCA probe molecules on the MSM, which is further supported by a low-angle p-XRD pattern, as depicted in the ESM (Fig. S4a, inset graph). Further, the low-angle p-XRD confirms the hexagonal pore architecture with *p6mm* mesophase for the bare MSM and Sensor-I through the presence of diffraction peaks (2θ) at 0.94°, 1.53°, and 1.74° that corresponds to (1 0 0), (1 1 0),

and (2 0 0) reflections. The uninterrupted existence of these characteristic peaks even after probe (BDHCA) impregnation on the MSM template reflects the high structural stability and retention of the mesoporous network for Sensor-I. The low-angle p-XRD pattern (ESM, Fig. S4b, inset plot) for Sensor-II, i.e., ATDBD functionalized MPM template, concedes a single intense peak at 0.8° (2θ), thus confirming the existence of mesopore channels across the continuous macro-porous polymer monolith network.

The surface area and porosity of the MSM template, Sensor-I, and Sensor-II are determined by BET and BJH methods by using liquid N_2 as adsorbate with respect to increasing relative pressure (P/P_o) till 0.999. The nitrogen adsorption/desorption isotherm pattern for MSM template, Sensor-I, and Sensor-II, are shown in the ESM (Section VI; Fig. S4(c-d)). The isotherm pattern for MSM, Sensor-I, and Sensor-II did not show any steep rise in the low-pressure region, i.e., P/P_o (0.01–0.5), which confirms the absence of micropores. However, the shape of the isotherm between ($0.5 > P/P_o < 0.8$) envisages a type-IV pattern, companied by an H1 hysteresis loop that confirms the existence of cylindrical mesopores with cage-like architecture. It is noticed that the bare MSM template reveals a surface area value of 445.42 m^2/g, with a pore volume and diameter value of 0.70 cm^3/g and 3.40 nm, respectively. However, for Sensor-I, upon BDHCA probe anchoring the MSM shows a significant decline in the surface area (334.84 m^2/g), pore size (0.66 cm^3/g), and pore diameter (3.28 nm), thus confirming the inclusion of probe molecules into MSM template, without altering the hysteresis loop and isotherm pattern. In the case of Sensor-II, the ATDBD functionalized MPM shows an H1 hysteresis loop and a type-V isotherm that signifies the existence of mesopores across the disoriented macroporous network. The cross-linked polymer network reveals a surface area of 56.98 m^2/g and a pore size of 0.16 cm^3/g. Due to the macroporous framework, Sensor-II exhibits a superior pore diameter value of 7.09 nm, which eventually enhances the effective percolation of the Co(II) ions to the active sites (probe chelating), thus offering faster response kinetics.

The surface morphology and structural architecture of the sensor materials are studied by FE-SEM and HR-TEM analysis. Figure 1a and b displays the FE-SEM imaging of MSM template reveal an interconnected porous network of continuously cage-shaped clusters that leads to the formation of a long-range 2D-monolithic pattern of highly ordered structural intergrowth network. The presence of rough surfaces of mesoporous architectures serves as an excellent host template for chromoionophoric probes, during ion-sensing. Figure 1c and d shows the TEM images of the MSM template, which reveals a well-organized 2D hexagonal pattern of honeycomb monolithic structure with a pore diameter of 3.40 nm, which is consistent with the BJH plot. The formation of 2D-hexagonal honeycomb arrays is assisted through the self-assembly of Pluronic F127 triblock copolymer molecules along with $Si(OEt)_4$ precursors. The solidification of inorganic-organic micelle assembly facilitates the formation of a highly ordered hexagonal mesoporous network of monolithic design. The stoichiometric addition of dodecane (as the swelling agent/non-polar microemulsion) accounts for the porosity features in terms of enlargement in pore diameter and volume. The existence of the hexagonal mesophase arrangement plays a crucial role in providing uniform and homogenous ordering of probe molecules, thus improving the overall analytical performance of solid-state sensor design. The calculated d-spacing value using a fast Fourier transform pattern (FFT) is in coherence with the low-angle p-XRD data. The elemental mapping (Fig. 1e, f) confirms the uniform distribution of Si and O atoms across the MSM template. Similarly, the EDAX spectra (Fig. 1g) shows the existence of the Si-O-Si framework that corroborates with the elemental mapping images. Further, the amorphous nature of silica monoliths is further confirmed by SAED (inset Fig. 1g) through the absence of bright spots, as projected earlier by p-XRD. For Sensor-II, the SEM images (Fig. 1h, i) reveal an interconnected porous framework with a rough surface morphology of a monolithic network, which is comprised of fused mesochannels within the uniform macroporous network. The TEM images (Fig. 1j, k) reveal a mesoporous chain network distributed uniformly across the macroporous structural framework. It also reveals the presence of bimodal pore (meso/macro) combinations thus facilitating a significant efficacy in propagating the target analytes to the active probe reaction sites that eventually transform into faster response kinetics for the sensor materials. The translucent polymer monolith shows a void-filled monolithic/single-blocked structure, which eases the diffusion process of the analytes through the bulk of the material. Hence, it is clear that the use of DMSO as a porogenic solvent followed by the temperature-controlled polymerization creates a highly ordered network of macroporous inner structures. Further, elemental mapping (Fig. 1l–o) confirms the functionalization of ATDBD with MPM. Similarly, the EDAX (Fig. 1p) spectra for Sensor-II confirm the existence of, oxygen, sulfur, nitrogen, and carbon elemental content across the porous polymer network, thereby substantiating the chemical functionalization of ATDBD. In addition, the amorphous character of Sensor-II was confirmed from the SAED pattern (inset Fig. 1p).

^{29}Si and ^{13}C CPMAS solid-state NMR measurements are performed to investigate the structural integrity and functional groups that are associated with Sensor-I and Sensor-II. ^{29}Si NMR spectra (Fig. 2a) for the MSM template reveals three peaks at − 93 (Q2), − 102 (Q3), and − 111 (Q4) ppm that refers to $Si(OSi)_2(OH_2)$ (Q2), $Si(OSi)_3(OH)$ (Q3) and $Si(OSi)_4$ (Q4), respectively, thereby confirming the existence of pristine silica network [34]. For Sensor-I, the abovementioned characteristic peaks show a decrease in their

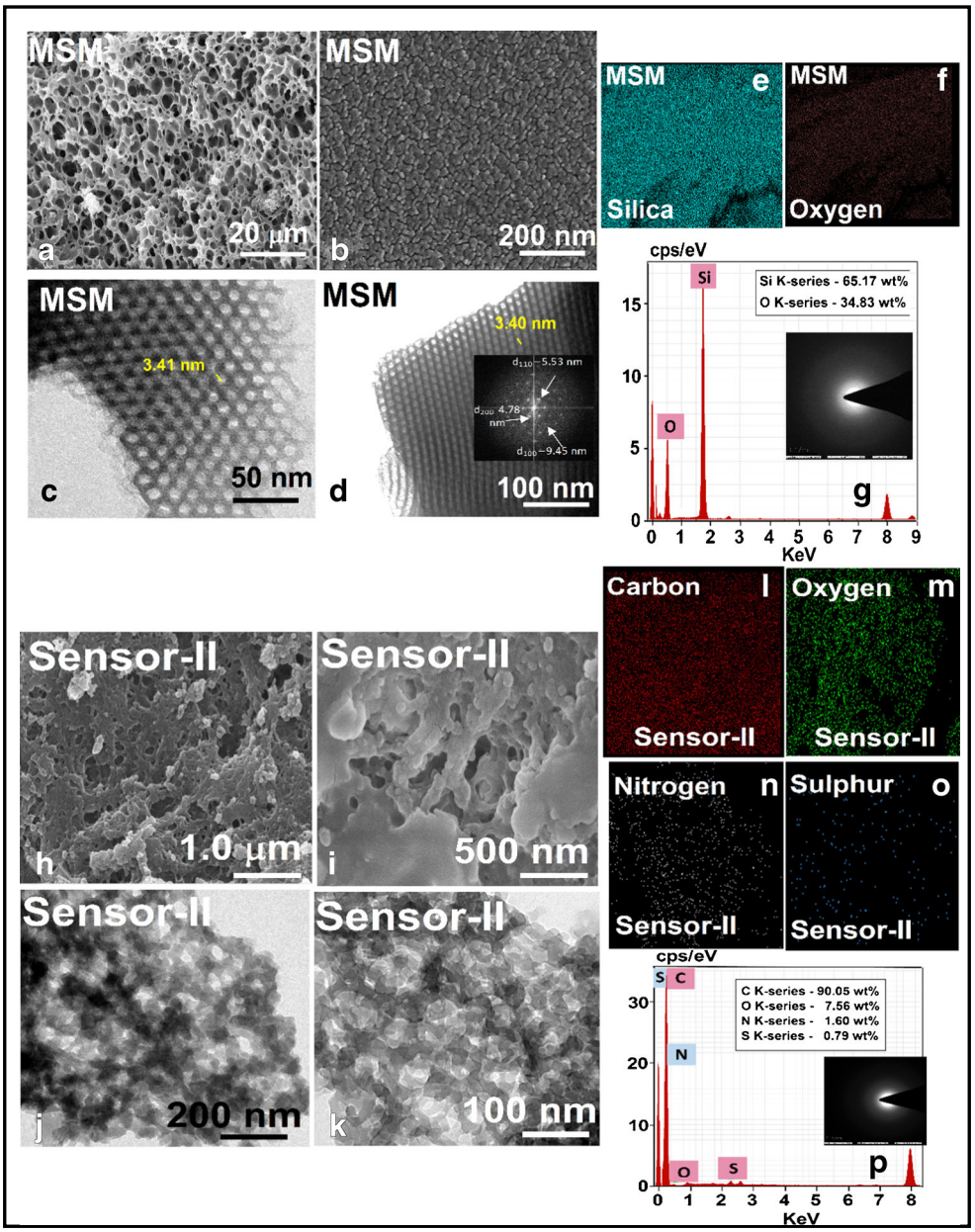

Fig. 1 **a**, **b** FE-SEM images, **c**, **d** HR-TEM images, **e**, **f** Elemental mapping, **g** EDAX & SAED (inset) data of MSM template, and **h**, **i** FE-SEM images, **j**, **k** HR-TEM images, **l–o** elemental mapping, **p** EDAX & SAED (inset) data of Sensor-II

intensity, thus substantiating the probe anchoring on MSM [35]. Moreover, the absence of any other peaks in the range of − 53 to − 73 ppm confirms the absence of the R-Si bond on the surface silica matrix. In the case of Sensor II, the ^{13}C CPMAS NMR spectra (Fig. 2b) reveal a resonance peak at 177 ppm that corresponds to the ester carbonyl groups of EGDMA cross-linker. The presence of multiple peaks in the range of 18–63 ppm corresponds to the alkyl functional groups present in the EGDMA backbone [36]. However, the new peak observed at 163 ppm correlates to the aromatic moiety of the ATDBD probe (monomers) functionalized with the EGDMA cross-linkers, thereby confirming the covalent bonding of the monomeric ATDBD probe with the EGDMA cross-linker, by the polymerization process [37]. In this line, the FT-IR spectra for the MSM template, Sensor-I, and Sensor-II are represented in Fig. 2c. For the bare MSM, the broad peak at 3445 cm^{-1} reflects the stretching vibrational frequency of the -OH group that is present on the surface of the silica monolithic framework. The peak at 1075 cm^{-1} corresponds to the Si-O-Si asymmetric stretching vibrations and further this vibrational frequency is shifted to 1066 cm^{-1} upon physical anchoring of BDHCA on MSM template (Sensor-I). The resonance peaks at 799 and 476 cm^{-1} for bare MSM corresponds to symmetric stretching and bending vibrational frequencies of the Si-O-Si group. However, upon BDHCA probe anchoring their respective vibrational frequencies are shifted to 797 cm^{-1} and 469 cm^{-1}. The slight shift in IR vibration frequencies signifies the physical interaction of

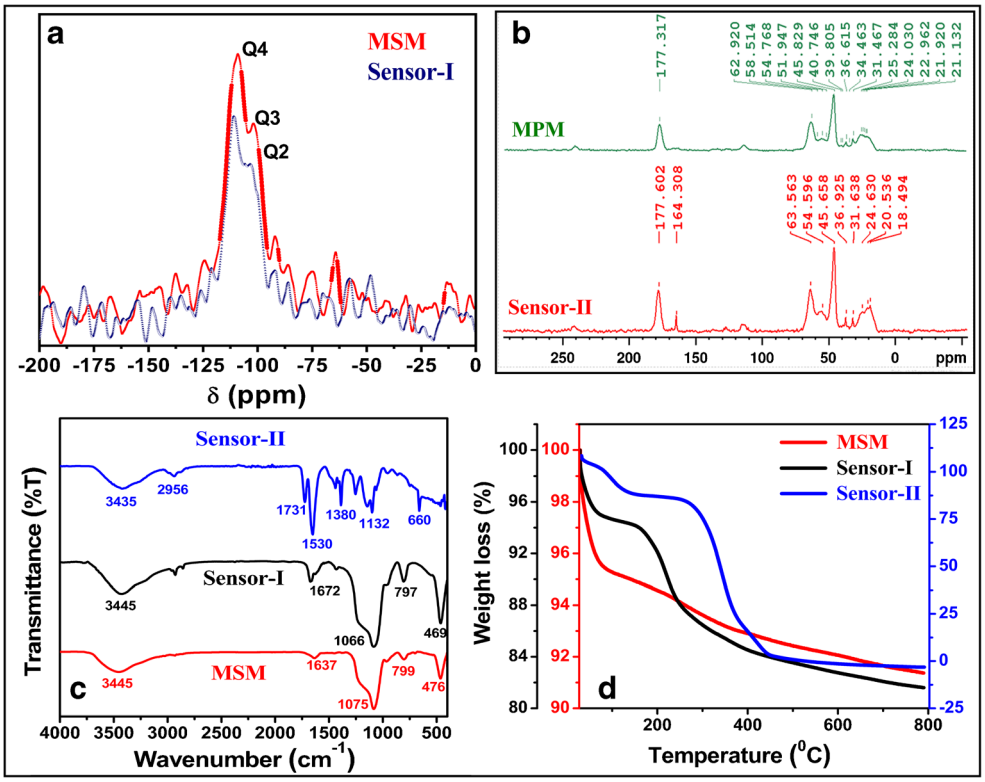

Fig. 2 CPMAS solid-state NMR, **a** ^{29}Si spectra for MSM and Sensor-I, **b** ^{13}C spectra for MPM and Sensor-II, **c** FT-IR spectra, and **d** TGA plot for MSM template, Sensor-I, and Sensor-II

BDHCA molecules with the silica network. For Sensor-II, the broad diffusion peak at 3435 cm^{-1} corresponds to O-H stretching vibrational frequency of water molecules that are adsorbed on the MPM. The peaks at 1380 cm^{-1} and 660 cm^{-1} correspond to C-H and C-S bending vibrations, respectively, of the ATDBD probe. Likewise, the increase in the peak intensity at 1530 cm^{-1} confirms the presence of -N=N- linkage in the polymer network, thereby substantiating the functionalization of the ATDBD probe [38].

TG analysis for the MSM template, Sensor-I, and Sensor-II are performed under N_2 atmosphere in the range of 30–800 °C, at a temperature ramping rate of 10 °C/min, as indicated in Fig. 2d. For the bare MSM, a net weight loss of 4.6% in the temperature range of 30–150 °C is attributed to the evaporation of water molecules that are adsorbed on the sensor surface. Furthermore, a weight loss of 2.4% is observed between 150 to 450 °C, which is associated with the thermal disintegration of traces of inorganic and organic impurities. However, for BDHCA loaded MSM (Sensor-I), the first stage weight loss is only 2.7%, which shows the low presence of adsorbed water molecules. However, in the second stage, a weight loss of 6.5% is attributed to the thermal disintegration of the anchored probe molecules. The thermogram reveals a difference in weight loss of ~4.1% between the MSM and Sensor-I samples, which corresponds to 0.201 mmol of BDHCA probe coated per gram of MSM. The obtained data corroborates the experimental value of 0.196 mmol/g, as discussed earlier in the experimental section and also in the ESM. In the case of Sensor-II, the TGA reveals a cumulative weight loss of 8.1% till 450 °C, which is associated with the disintegration of the organic polymer network.

The existence of various elements and their relative oxidation states in the fabricated Co(II)-sensory systems are evaluated using XPS analysis. Figure 3a reveals the XPS (wide-range) spectra for Co(II) complexed Sensor-I and Sensor-II materials, which reveals the elemental presence of Si, O, and Co for Sensor-I, and C, O, N, S, and Co for Sensor-II, respectively. Figure 3b shows the deconvoluted Co*2p* spectra with predominant peaks observed at 782.7 and 797.4 eV refers to Co^{2+} $2p_{3/2}$ and $2p_{1/2}$ orbital states, respectively. The additional existence of low intense satellite peaks at both 787.7 and 801.6 eV further confirms the divalent oxidation state of cobalt ions in both Sensor-I and Sensor-II materials [27]. Figure 3c shows the deconvoluted spectra of Si$2p_{3/2}$ and Si$2p_{1/2}$ orbital states in Sensor-I at 102.8 and 104.5 eV, respectively, thus confirming the existence of Si-O-Si and $Si(OH_2)$ linkage, with Si^{4+} oxidation states. Figure 3d depicts the deconvoluted O*1s* spectra that are reciprocated by two distinct peaks, one at 530.2 eV for the ionic oxygen located in the Si-O-Si network, and the other at 532.01 eV, which is assigned to the surface Si-OH groups [39]. For Sensor-II, the high-resolution deconvoluted spectra for C*1s*, O*1s*, N*1s*, and S*2p* orbitals are shown in Fig. 3e–h. In the C*1s* spectra, the peaks at 284.8, 286.0, and 288.9 eV indicate the presence of carbon backbone in the polymer matrix in the form of C-C, C-O, and O-C=O groups, respectively. The deconvoluted O*1s*

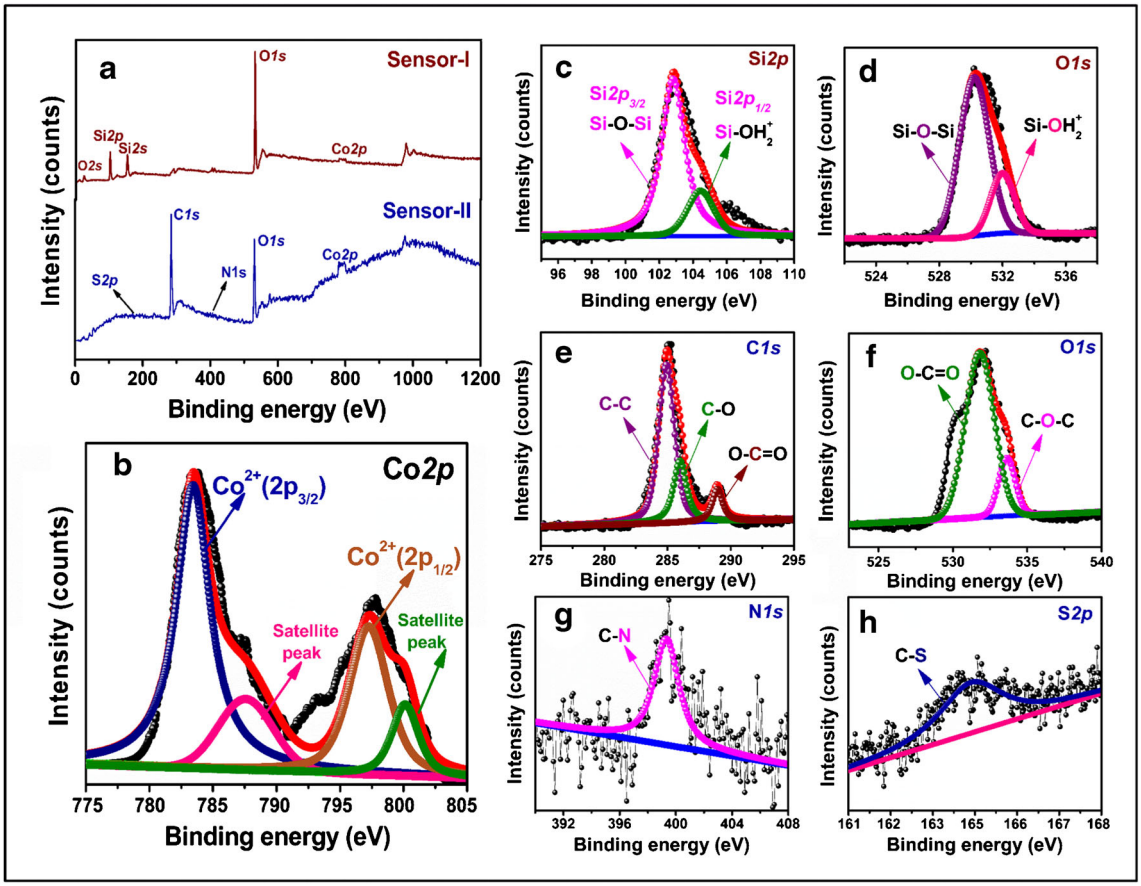

Fig. 3 **a** XPS wide range survey spectra for Sensor-I and Sensor-II, **b** deconvoluted XPS spectra for *Co2p* orbital state of cobalt sensor, **c**, **d** deconvoluted high resolution XPS spectra for *Si2p* and *O1s* orbital states of Sensor-I, **e**–**h** deconvoluted high resolution spectra for *C1s*, *O1s*, *N1s* & *S2p* orbital states of Sensor-II

orbital state proffers an intense peak around 531.8 eV corresponding to the O-C=O unit and a low-intensity peak at 533.6 eV is ascertained to the C-O-C unit that is present across the polymer framework. The deconvoluted N*1s* and S*2p* spectra show characteristic peaks at 399.0 and 164.2 eV that correspond to C-N and C-S groups from an allyl functional ATDBD monomeric ligand [40].

Optimization of sensor analytical performance

The influence of solution pH is essential for the detection and determination of the target (Co(II)) analyte with the materials of the proposed sensor. For this, the sensing efficiency of sensors (I and II) is monitored at various solution pH (2.0–9.0), at a specific Co(II) concentration (100 ppb), as presented in Fig. 4a. The solution pH reciprocal ion-signal response plot shows that the sensors exhibit maximum signal response at a solution pH of 8.0, for Co(II) sensing (considering the pKa > 7.0, for both BDHCA and ATDBD). However, under mild acidic solutions, the inadequate signal response reflected by both the sensor materials is correlated to the protonation of anchored organic probe ligand molecules that prompts repulsive interaction for Co(II), during the complexation process. In the case of solution pH > 8.0, the formation of cobalt hydroxide species hinders the sensing process, thereby decreasing the signal response. Thus, considering the importance of solution pH during the sensing process, the optimized pH conditions are maintained even during monitoring of other physicochemical factors. In this line, the influence of solution temperature has been studied by equilibrating the sensor materials with Co(II) (100 ppb) ions, from 20 to 40 °C, as shown in Fig. 4b. The temperature-dependent plot reveals a maximum signal response for Co(II) at 35 °C and 30 °C, for Sensor-I and Sensor-II, respectively. Interestingly, the lower temperature for Sensor-II is attributed to the presence of a macroporous network design that promotes greater diffusion of Co(II) ions to the probe-chelating sites for ion-complexation/sensing. The cobalt ion-sensing kinetics increases with solution temperature due to the increase in thermal energy that eventually enhances the metal ion diffusion kinetics, thus leading to faster complexation with the active sites of the anchored probe molecules.

In this manner, the critical amount of ligand impregnation/functionalization with the monolithic templates for effective metal ion sensing is depicted in Fig. 4c. For the sensing of

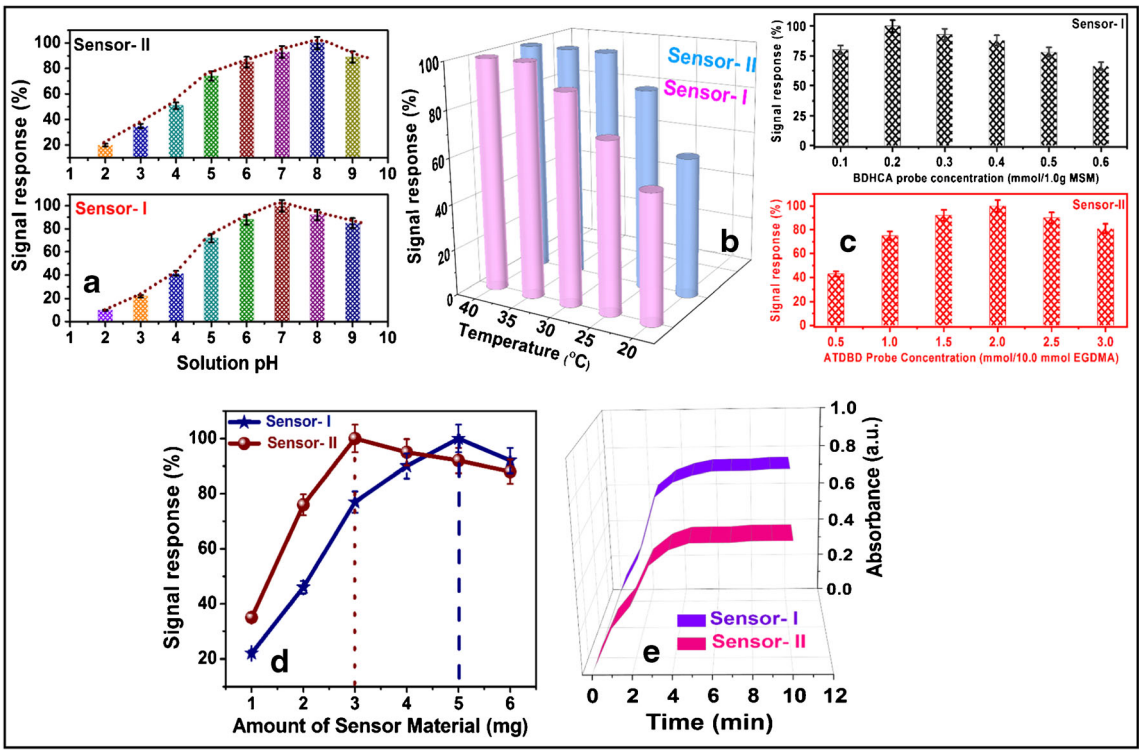

Fig. 4 Influence of **a** pH (≤ 5 min, RSD: 2.31%), **b** temperature (≤ 5 min, RSD: 2.45%), **c** probe concentration (≤ 5 min, RSD: 2.82%), **d** sensor quantity (≤ 5 min, RSD: 2.74%), **e** response kinetics (RSD: 2.82%), of Sensor-I and Sensor-II towards Co^{2+} sensing

Co(II) (100 ppb), 0.196 mmol of BDHCA probe coated MSM template (Sensor-I) provided the best signal response. In the case of Sensor-II, the plot shows that the functionalization of 2.0 mmol of ATDBD monomer reveals better signal response for the quantitatively sensing of Co(II) (100 ppb). For both sensor materials, a poor response is observed below the specified probe concentration, which is attributed to the inadequate availability of probe molecules for effective complexation with the available Co(II) ions. However, with excess probe concentration (beyond the optimum level), the initial/original color of the non-complexed (excess) probe molecules interferes with the color transitions resulting from the ligand-to-metal ion charge transfer transitions, thus hampering the sensitivity factor, particularly while dealing with ultra-trace concentrations of Co(II) ions.

Similarly, the role of sensor quantity on the ion-sensing process is depicted in Fig. 4d. The plot reveals an optimum sensor quantity of 5.0 and 3.0 mg for Sensor-I and Sensor-II, respectively, for the quantitative detection of ultra-trace concentration of Co(II). However, below the threshold values, both the sensors reveal a weak signal response, which is associated with the inadequate active sites for ion-complexation. Similarly, a low signal intensity is observed beyond the optimum sensor quantity is attributed to the excess probe molecules, which hamper the intensity of color transitions arising from Co(II)-probe complexation. These observations not only confirm the necessity of sensor/probe quantity for metal ion recognition but also provoke the knowledge about the stoichiometric complexation mechanism of the proposed sensory system. The complexation ratio of Co(II) ions with the probe molecules is monitored by using Job's method and NMR titration experiments. From the obtained results, it is evident that both [Co^{2+}-BDHCA] and [Co^{2+}-ATDBD] complexes are at a 1:1 ratio, as discussed in the ESM (Section IV). Finally, the metal ion response kinetics associated with proposed sensors has been studied as a function of equilibration time, under optimized working conditions, as depicted in Fig. 4e. The figure illustrates a saturated signal response time of 6.0 and 4.0 min for Sensor-I and Sensor-II, respectively. For Sensor-II, a slightly faster response kinetics with respect to Sensor-I is associated with the bimodal (macro/meso) porosity of the polymer monoliths that promotes faster diffusion kinetics in comparison with the use of mesoporous silica monolith–based Sensor-I. Overall, the short time-span of analysis confirms the possibility of the proposed sensors for real-time on-site monitoring of samples.

Analytical performance and practical applications

However, for qualitative and quantitative validation of the sensory systems, the studies are performed using a Co(II) concentration range of 0–200 ppb, at ambient conditions. The obtained results are quantified using UV-Vis-DRS spectral analysis, apart from naked-eye comparison, as depicted in Fig. 5a, b. The spectra response plot in the case of Sensor-I

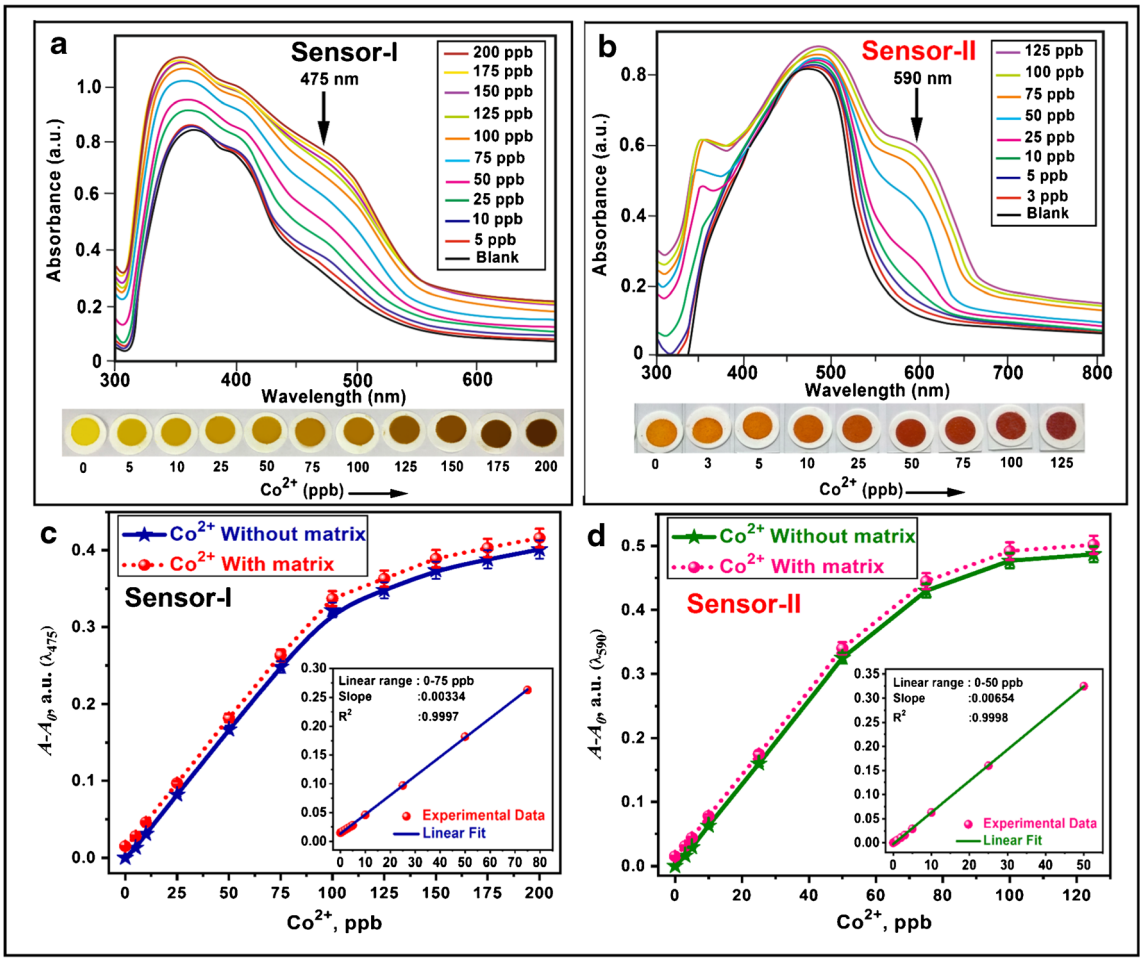

Fig. 5 **a**, **b** UV-Vis-DRS signal response and naked-eye color transition and **c**, **d** calibration plot (Inset plot signifies the linear fit in the linear response range, with RSD of 2.67% and 2.82% from triplicate analysis) for various concentration of Co^{2+} ions in the presence and absence of interfering foreign (matrix) ions (Cations: Na^{+}, K^{+}, Ca^{2+}, Mg^{2+}, Ni^{2+}, Mn^{2+}, Fe^{2+}, Cu^{2+}, Zn^{2+}, Pb^{2+}, Hg^{2+}, and Cd^{2+}. Anions: Cl^{-}, NO_3^{-}, SO_4^{2-}, PO_4^{3-}, CO_3^{2-}, HCO_3^{-}, and F^{-}, within their tolerance limit), using Sensor-I and Sensor-II, respectively

reveals an increase in relative reflection intensity at 475 nm (λ_{max}) that is associated with a color transition from pale-yellow to greenish-brown, with increasing Co(II) concentrations. For Sensor-II, the gradual color transformation from pale orange to deep red with increasing Co(II) concentration has been monitored at 590 nm (λ_{max}). The bathochromic shifts that are associated with resulting color transitions in the case of both Sensor-I and Sensor-II are ascribed to ligand-to-metal ion charge transfer mechanism. The calibration plot (Fig. 5c, d) towards Co(II) detection in the presence (dotted line) and absence (solid line) of other competitive metal ions (matrix) reflects the linear response range of the sensor materials for the qualitative/quantitative determination of Co(II). The plot shows a linear correlation (r^2 – 0.999) in the Co(II) concentration range of 0.25–100 ppb and 0.25–50 ppb, for Sensor-I and Sensor-II, respectively, with a dynamic response range up to 200 ppb and 125 ppb. Based on the linear plot, the limit of detection (LOD) and quantification (LOQ) are calculated using the equation $3\sigma/m$ and $10\sigma/m$, respectively, where "σ" is the standard deviation (3.3×10^{-4} and 3.2×10^{-4}) for pentaplicate measurements of blank sensors, and "m" is the slope (0.197 and 0.385) in the linear concentration range for Sensor-I and Sensor-II, respectively. The calculated LOD and LOQ for Sensor-I is 0.29 ppb and 1.03 ppb, respectively and for Sensor-II, it is 0.15 ppb and 0.51 ppb, respectively. For data reliability, all the metal concentration studies analyzed are subjected to triplicate measurements, with a RSD of ≤ 2.82%. The pictorial presentation of the naked-eye detection of Co(II) in the sub-ppb range using Sensor-I and II, are included in the ESM (Section VII). In order to showcase the superiority of the proposed sensory systems, a comparison table has been provided in Table 1, based on the analytical features of literature reported liquid and solid-state sensors for Co(II) sensing [27–33].

Table 1 Comparison table in terms of the analytical parameters of the proposed sensors with respect to literature reports

S. No.	Sensing Method	Response Range (ppb)	LOD (ppb)	Ref.
1.	Solid-state colorimetric sensing of Co^{2+} using silica monolith modified 8-(4-n-dodecyl-phenylazo),2,4-quinolinediol.	0.0-90	0.88	[27]
2.	Solid-state sensing of Co^{2+} using silica monolith modified with, (i) 2-nitroso-1-naphthol, (ii) bis[bis(carboxymethyl) aminomethyl]fluorescein, and (iii) pyrogallol red.	0.0-2000	0.51 0.22 0.33	[28]
3.	Solid-state colorimetric sensing of Co^{2+} using silica monolith modified with N,N-disalicylidene-4,5-dimethylphenylenedene.	0.0-6000	0.33	[29]
4.	Solid-state colorimetric sensing of Co^{2+} using silica monolith modified with di(3-carboxysalicylidene)-3,4diamino-5-hydroxypyrazole.	0.0-2000	0.24	[30]
5.	Solid-state colorimetric sensing of Co^{2+} using, (i) silica monolith modified with 2-(4-butylphenyl)diazenyl)-2-hydroxybenzylidene) hydrazine-1-carbothioamide (BDHCA), and (ii) 4-((5-(allylthio)-1,3,4-thiadiazol-2-yl)diazenyl)benzene-1,3-diol (ATDBD) functionalized porous polymer monolith.	0.0-200 0.0-125	**0.29** **0.15**	**Present work**

In addition to this analytical performance, the significant advantage of the proposed solid-state sensor designs is their ability to tune-up their ion-selectivity for Co(II) targeting amidst foreign ions. To investigate the impact of matrix constituents on Co(II) ion-selectivity, both Sensor-I and Sensor-II are subjected to equilibration with an excess of common cations and anions to the sensor materials under the optimized conditions. Here, the matrix refers to the presence of foreign ions/species that could potentially interfere in the sensing of Co(II) ions. The matrix tolerance limit of the proposed sensors is shown in Table 2, and their ion-selectivity is depicted in Fig. 6. The ion-selectivity studies reveal negligible changes to the signal intensity of $[Co\text{-}Probe]^{n+}$ complex amidst a wide range and concentrations of matrix constituents. In the case of sensor-1, the presence of Cu^{2+} ions at concentrations ≥ 5.5 ppm showed a significant disturbance in the Co(II) ion-sensing, which is eliminated by the addition of 0.25 mM thiosulphate thereby increasing its tolerance limit up to 160 folds, as depicted in the ESM (Section VIII). In the case of Sensor-II, a significant interference is observed from Ni^{2+} ions at concentrations ≥ 6.1 ppm, which can be eliminated by the

Table 2 Tolerance limits of matrix ions during the sensing of trace concentrations of Co(II) ions

Electrolytes	Tolerance Limit (ppm)		Cations	Tolerance Limit (ppm)	
	Sensor-I	Sensor-II		Sensor-I	Sensor-II
NaCl	5200	5750	Cr^{6+}	9.7	10.5
Na_2SO_4	2500	2850	Ni^{2+}	10.0	6.1[#]
Na_3PO_4	3250	4800	Cu^{2+}	5.5[#]	9.5
$MgCO_3$	670	720	$Fe^{2+/3+}$	11.5	10.5
$Ca(HCO_3)_2$	350	450	La^{3+}	10.0	10.0
NaF	300	500	Pb^{2+}	9.4	9.0
$NaHCO_3$	250	450	Zn^{2+}	12.0	15.5
KNO_3	3750	4200	Mn^{2+}	14.0	11.5
KSCN	200	150	Hg^{2+}	10.0	8.8
KBr	750	1200	Cd^{2+}	8.5	9.0
			Al^{3+}	12.0	14.0
			Zn^{2+}	9.5	15.5
			As^{3+}	12.0	14.0

[#] Tolerance limit in the presence of masking agents

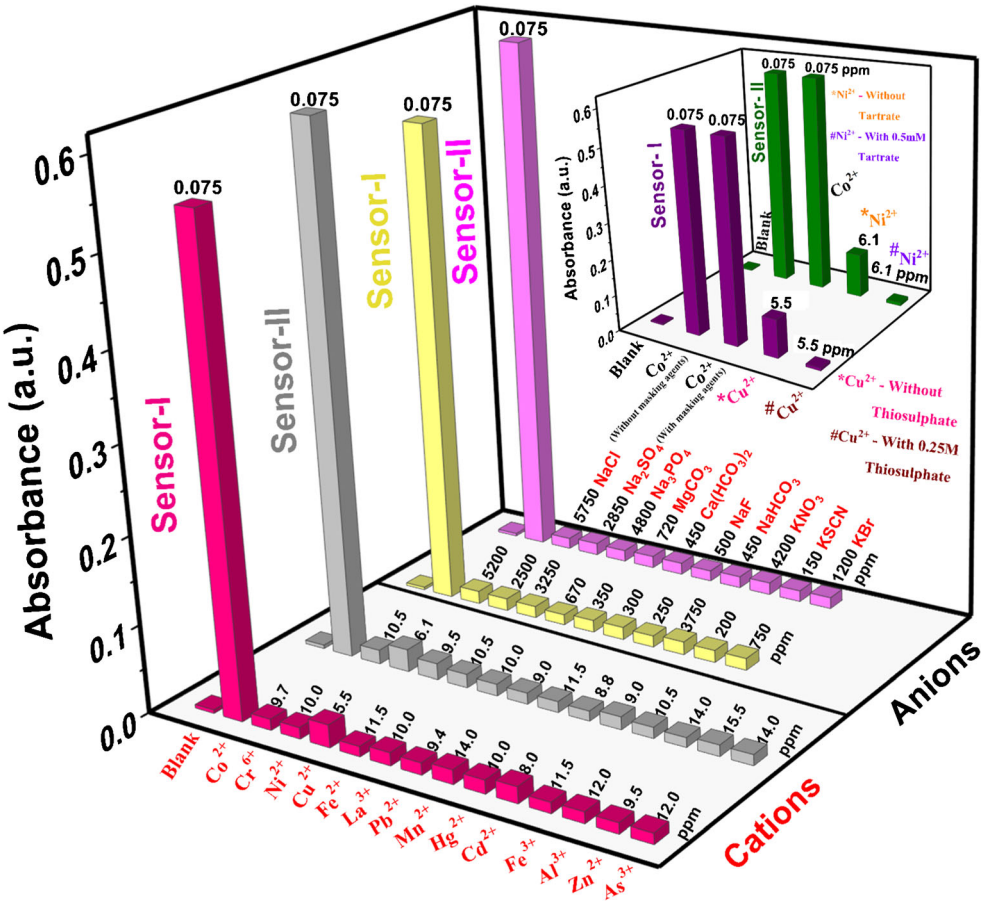

Fig. 6 Ion-selectivity (RSD: 2.82%) for Sensor-I and Sensor-II towards Co(II) sensing. Inset plot signifies the relative signal response of Sensor-I and Sensor-II pertaining to Co(II), Cu(II), and Ni(II), in the absence and presence of masking agents (0.25 mM thiosulphate and 0.50 mM tartrate)

addition of 0.50 mM tartrate as a masking agent, thereby eliminating its interference up to 200-folds of concentrations, with respect to Co(II) concentration. The analytical results reveal that the proposed sensors exhibit remarkable ion-selectivity in capturing trace levels of Co(II) ions, thus paving the way for their practical utility. The complex formation mechanism of probe molecules with Co(II) ions and the resulting ion-selectivity are discussed in the ESM (Section IX).

The practical application and real-time challenges that are associated with the proposed sensors have been extensively studied using environmental water and pre-treated industrial wastewater samples, and also with scarp Li-ion batteries, as tabulated in Table 3. The analysis of the abovementioned samples using our proposed sensor materials reveals a cobalt ion recovery value of ≥ 103.62% (RSD ≤ 2.07%), for triplicate analysis. The analytical data reflects on the data

Table 3 Capturing of Co(II) from spiked environmental and industrial samples using the proposed sensors

Source	Sample Composition†	Co^{2+} Spiked† ppb)	Co^{2+} Capture (Sensor-I)	Co^{2+} Capture (Sensor-II)
Groundwater	Ni/Cu/Zn (≤ 0.14); Mn/Fe (≤ 5.2); Na/K/Mg/Ca (≤ 530); Cl^-/HCO_3^- (≤ 470); $F^-/NO_3^{2-}/PO_4^{3-}$ (≤ 75); Co (n.d) ppm	0.0	0	0
		10.07	$09.6^a \pm 1.5^b$	$11.1^a \pm 1.0^b$
		25.11	$26.2^a \pm 1.8^b$	$25.7^a \pm 1.5^b$
Lake Water	Ni/Cu/Mn (≤ 0.08); Ca/Mg/Na/K (≤ 320); $F^-/NO_3^-/PO_4$ (≤ 120); Fe/Zn (≤ 15.2); SO_4^{2-}/Cl^- (≤ 220) Co (n.d) ppm	0.0	0	0
		10.11	$11.2^a \pm 0.9^b$	$10.8^a \pm 1.1^b$
		30.17	$30.5^a \pm 1.5^b$	$29.0^a \pm 2.0^b$
Electronics Industry Wastewater	Cu/Mn/Al (≤ 7.2) Pb/Cd/Hg (≤ 0.5); Fe/Mn (≤ 9.4); Co (n.d) ppb	0.0	0	0
		20.15	$20.6^a \pm 1.5^b$	$21.0^a \pm 1.2^b$
		50.22	$49.6^a \pm 0.7^b$	$51.7^a \pm 1.5^b$
Scrap Li-ion Battery	Li (5.79); Co (50.07); Ni (2.16); Mn (3.74); Cu (0.72); Al (0.78); Fe (1.12) ppb	0.0	$48.2^a \pm 2.4^b$	$48.9^a \pm 2.2^b$
		15.09	$65.5^a \pm 1.4^b$	$66.2^a \pm 1.9^b$
		25.13	$73.1^a \pm 2.2^b$	$73.7^a \pm 2.0^b$

[a] Triplicate measurements; [b] standard deviation; † data based on ICP-MS analysis; *n.d.* not detected

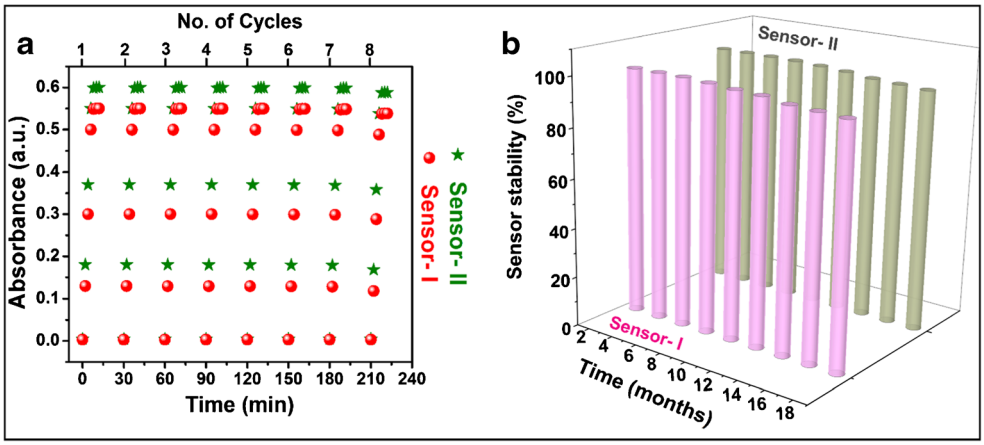

Fig. 7 **a** Reusability (RSD: 2.32%) and **b** durability studies (RSD: 1.54%), for Sensor-I and Sensor-II towards Co(II) sensing

reproducibility and reliability of the proposed sensory systems for the quantitative sensing of cobalt ions. Furthermore, to reduce the cost factor, reusability studies are performed with the proposed solid-state sensors. The reusability plot depicting the performance of the sensors is discussed in Fig. 7a. The captured cobalt ions are eluted with 2 mL of 0.01 M HCl, and the eluents are analyzed by ICP-MS. The analytical data ensures the complete regeneration of the sensor materials to their original state followed by the recapturing of Co(II) ions upon subsequent equilibration that lasted for more than seven reuse cycles. However, the efficiency of the regenerated sensor material is found to decrease after eight cycles due to the gradual disintegration of probe molecules from sensor materials after several courses of acid and water treatment. To analyze the data reproducibility, day-to-day and batch-to-batch analyses of sensor performance reveal an RSD of < 1.45% and < 2.65%, respectively. Similarly, the sensor durability is analyzed by storing for about 18 months, with a periodic assessment of their sensing performance. The efficiency of the sensor performance and its time-dependent durability are discussed in Fig. 7b. The results show that the sensor materials exhibit excellent stability without loss in their sensing efficacy/optical properties, even under different physical/chemical environments (pH, humidity, and light), over the monitored period. Overall, the design of highly ordered porous monolithic architectures along with tailor-made probe molecules not only provides excellent sensitivity and selectivity but also offers high durability and reusability features.

Conclusion

The stereo-specific anchoring of probe molecules on the porous monolithic silica and polymer templates offer two solid-state colorimetric ion-sensors that exhibit excellent selectivity and sensitivity, for the naked eye sensing of Co(II) ions. The silica and polymer monolith–based sensors exhibit different binding mechanisms with the probe molecules, i.e., BDHCA and ATDBD, respectively, with the former exhibiting a physical adsorption via non-covalent (van der Waals) interaction, and the latter covalently integrating the probe (functional monomer) as a part of the porous polymer monolithic network through free radical polymerization. The surface and structural properties of the fabricated solid-state sensors are characterized using various microscopic, spectroscopic, and diffraction techniques, which confirms the presence of a highly ordered structural network with high surface area and greater pore properties. The mesoporous 2D-hexagonally patterned honeycomb structure of silica monolith allows uniform dispersion of probe molecules thus enhancing the ion-sensing kinetics (≤ 5 min). The macro-/meso-pore combined bimodal alignment of polymer monoliths not only promotes faster sensing but also enhances the sensitivity factor. It is inferred that the structural properties of the monolithic templates along with the probe molecules act as a decisive factor towards the ion-selectivity, apart from the rapid transport of the target analytes to the binding sites through the sensor pore cavities. The superior ion-sensitivity with proposed monolithic sensory is attributed to the restricted spatial (structural) orientation of the probe molecules within the confined cavity-like porous networks of the silica/polymer monolith. The practical utility of the sensor materials has been tested with surface water and certified industrial samples, to confirm their real-time monitoring efficiency for ultra-trace levels of Co(II) ions. The proposed sensor materials are cost effective, along with features of reusability, durability, and data reliability.

Supplementary Information The online version contains supplementary material available at https://doi.org/10.1007/s00216-021-03255-1.

Acknowledgements The authors thank Sri Sai Company for providing the scrap Li-ion battery and also CVR Labs for sample analysis.

Funding This study was financially supported by SERB (SB/FT/CS-051/2014), and VIT (Institute Seed Grant 2019).

Declarations

Conflict of interest The authors declare no competing interests.

References

1. Ullah N, Mansha M, Khan I, Qurashi A. Nanomaterial-based optical chemical sensors for the detection of heavy metals in water: recent advances and challenges. TrAC - Trends Anal Chem. 2018;100:155–66. https://doi.org/10.1016/j.trac.2018.01.002.
2. Zhang L, Peng D, Liang RP, Qiu JD. Graphene-based optical nanosensors for detection of heavy metal ions. TrAC - Trends Anal Chem. 2018;102:280–9. https://doi.org/10.1016/j.trac.2018.02.010.
3. Mudhoo A, Ramasamy DL, Bhatnagar A, Usman M, Sillanpää M. An analysis of the versatility and effectiveness of composts for sequestering heavy metal ions, dyes and xenobiotics from soils and aqueous milieus. Ecotoxicol Environ Saf. 2020;197:110587. https://doi.org/10.1016/j.ecoenv.2020.110587.
4. Li J, Guo L, Zhao N, Yang X, Yi R, Li K, et al. Determination of cobalt in low-alloy steels using laser-induced breakdown spectroscopy combined with laser-induced fluorescence. Talanta. 2016;151:234–8. https://doi.org/10.1016/j.talanta.2016.01.023.
5. Au-Yeung HY, New EJ, Chang CJ. A selective reaction-based fluorescent probe for detecting cobalt in living cells. Chem Commun. 2012;48:5268–70. https://doi.org/10.1039/c2cc31681a.
6. Liu Z, Jia X, Bian P, Ma Z. A simple and novel system for colorimetric detection of cobalt ions. Analyst. 2014;139:585–8. https://doi.org/10.1039/c3an01845h.
7. El-Safty SA, Prabhakaran D, Ismail AA, Matsunaga H, Mizukami F. Three-dimensional wormhole and ordered mesostructures and their applicability as optically ion-sensitive probe templates. Chem Mater. 2008;20:2644–54. https://doi.org/10.1021/cm701966c.
8. Zhu H, Fan J, Wang B, Peng X. Fluorescent, MRI, and colorimetric chemical sensors for the first-row d-block metal ions. Chem Soc Rev. 2015;44:4337–66. https://doi.org/10.1039/c4cs00285g.
9. Ryu KY, Lee SY, Park DY, Kim SY, Kim C. A novel colorimetric chemosensor for detection of Co^{2+} and S^{2-} in an aqueous environment. Sensors Actuators B Chem. 2017;242:792–800. https://doi.org/10.1016/j.snb.2016.09.180.
10. Maity D, Govindaraju T. Highly selective colorimetric chemosensor for Co^{2+}. Inorg Chem. 2011;50:11282–4. https://doi.org/10.1021/ic2015447.
11. Song EJ, Kang J, You GR, Park GJ, Kim Y, Kim SJ, et al. A single molecule that acts as a fluorescence sensor for zinc and cadmium and a colorimetric sensor for cobalt. Dalt Trans. 2013;42:15514–20. https://doi.org/10.1039/c3dt51635k.
12. Kang SM, Jang SC, Kim GY, Lee CS, Huh YS, Roh C. A rapid in situ colorimetric assay for cobalt detection by the naked eye. Sensors (Switzerland). 2016;16:1–10. https://doi.org/10.3390/s16050626.
13. Vashisht D, Kaur K, Jukaria R, Vashisht A, Sharma S, Mehta SK. Colorimetric chemosensor based on coumarin skeleton for selective naked eye detection of cobalt (II) ion in near aqueous medium. Sensors Actuators B Chem. 2019;280:219–26. https://doi.org/10.1016/j.snb.2018.10.020.
14. Liu Z, Wang W, Xu H, Sheng L, Chen S, Huang D, et al. A "naked eye" and ratiometric chemosensor for cobalt(II) based on coumarin platform in aqueous solution. Inorg Chem Commun. 2015;62:19–23. https://doi.org/10.1016/j.inoche.2015.10.017.
15. Awual MR, Yaita T, Shiwaku H, Suzuki S. A sensitive ligand embedded nano-conjugate adsorbent for effective cobalt(II) ions capturing from contaminated water. Chem Eng J. 2015;276:1–10. https://doi.org/10.1016/j.cej.2015.04.058.
16. Awual MR, Islam A, Hasan MM, Rahman MM, Asiri AM, Khaleque MA, et al. Introducing an alternate conjugated material for enhanced lead(II) capturing from wastewater. J Clean Prod. 2019;224:920–9. https://doi.org/10.1016/j.jclepro.2019.03.241.
17. Li M, Gou H, Al-Ogaidi I, Wu N. Nanostructured sensors for detection of heavy metals: a review. ACS Sustain Chem Eng. 2013;1:713–23. https://doi.org/10.1021/sc400019a.
18. Zhang L, Fang M. Nanomaterials in pollution trace detection and environmental improvement. Nano Today. 2010;5:128–42. https://doi.org/10.1016/j.nantod.2010.03.002.
19. Yao Y, Tian D, Li H. Cooperative binding of bifunctionalized and click-synthesized silver nanoparticles for colorimetric Co^{2+} sensing. ACS Appl Mater Interfaces. 2010;2:684–90. https://doi.org/10.1021/am900741h.
20. Karami C, Taher MA. Colorimetric sensor of cobalt ions in aqueous solution using gold nanoparticles modified with glycyrrhizic acid. Plasmonics. 2018;13:1315–23. https://doi.org/10.1007/s11468-017-0635-9.
21. Umair M, Javed I, Rehman M, Madni A, Javeed A, Ghafoor A, et al. Nanotoxicity of inert materials: the case of gold, silver and iron. J Pharm Pharm Sci. 2016;19:161–80. https://doi.org/10.18433/j31021.
22. Ferdous Z, Nemmar A. Health impact of silver nanoparticles: a review of the biodistribution and toxicity following various routes of exposure. Int J Mol Sci. 2020;21:2375 https://www.mdpi.com/1422-0067/21/7/2375.
23. Liu G, Lu M, Huang X, Li T, Xu D. Application of gold-nanoparticle colorimetric sensing to rapid food safety screening. Sensors (Switzerland). 2018;18:1–16. https://doi.org/10.3390/s18124166.
24. El-Safty SA, Prabhakaran D, Ismail AA, Matsunaga H, Mizukami F. Nanosensor design packages: a smart and compact development for metal ions sensing responses. Adv Funct Mater. 2007;17:3731–45. https://doi.org/10.1002/adfm.200700447.
25. Kongasseri A, Sompalli NK, Modak VA, Mohanty A, Nagarajan S, Rao CVSB, et al. Solid-state ion recognition strategy using 2D hexagonal mesophase silica monolithic platform: a smart two-in-one approach for rapid and selective sensing of Cd^{2+} and Hg^{2+} ions. Microchim Acta. 2020;187:403. https://doi.org/10.1007/s00604-020-04363-y.
26. Shahat A, Hassan HMA, El-Shahat MF, El Shahawy O, Awual MR. A ligand-anchored optical composite material for efficient vanadium(II) adsorption and detection in wastewater. New J Chem. 2019;43:10324–35. https://doi.org/10.1039/c9nj01818b.
27. El-Safty SA. Functionalized hexagonal mesoporous silica monoliths with hydrophobic azo-chromophore for enhanced Co(II) ion monitoring. Adsorption. 2009;15:227–39. https://doi.org/10.1007/s10450-009-9171-z.
28. El-Safty SA, Awual MR, Shenashen MA, Shahat A. Simultaneous optical detection and extraction of cobalt(II) from lithium ion batteries using nanocollector monoliths. Sensors Actuators B Chem. 2013;176:1015–25. https://doi.org/10.1016/j.snb.2012.09.040.
29. Awual MR, Alharthi NH, Hasan MM, Karim MR, Islam A, Znad H, et al. Inorganic-organic based novel nano-conjugate material for effective cobalt(II) ions capturing from wastewater. Chem Eng J. 2017;324:130–9. https://doi.org/10.1016/j.cej.2017.05.026.
30. Shahat A, Awual MR, Naushad M. Functional ligand anchored nanomaterial based facial adsorbent for cobalt(II) detection and removal from water samples. Chem Eng J. 2015;271:155–63. https://doi.org/10.1016/j.cej.2015.02.097.
31. Nischang I, Causon TJ. Porous polymer monoliths: from their fundamental structure to analytical engineering applications. TrAC - Trends Anal Chem. 2016;75:108–17. https://doi.org/10.1016/j.trac.2015.05.013.

32. Svec F. Porous polymer monoliths: amazingly wide variety of techniques enabling their preparation. J Chromatogr A. 2010;1217:902–24. https://doi.org/10.1016/j.chroma.2009.09.073.
33. Kongasseri A, Sompalli NK, Rao CVS, Nagarajan S, Mohan AM, Deivasigamani P. Solid-state optical sensing of ultra-trace Hg^{2+} ions using chromoionophoric probe anchored silica monolithic architectures. Sensors Actuators B Chem. 2020;321:128558. https://doi.org/10.1016/j.snb.2020.128558.
34. Ismail AA. A selective optical sensor for antimony based on hexagonal mesoporous structures. J Colloid Interface Sci. 2008;317:288–97. https://doi.org/10.1016/j.jcis.2007.09.028.
35. Gomaa H, Shenashen MA, Yamaguchi H, Alamoudi AS, El-Safty SA. Extraction and recovery of Co^{2+} ions from spent lithium-ion batteries using hierarchical mesosponge γ-Al2O3 monolith extractors. Green Chem. 2018;20:1841–57. https://doi.org/10.1039/c7gc03673f.
36. Madikizela LM, Zunngu SS, Mlunguza NY, Tavengwa NT, Mdluli PS, Chimuka L. Application of molecularly imprinted polymer designed for the selective extraction of ketoprofen from wastewater. Water SA. 2018;44:406–18. https://doi.org/10.4314/wsa.v44i3.08.
37. Morgan DR, Kalachandra S, Shobha HK, Gunduz N, Stejskal EO. Analysis of a dimethacrylate copolymer (Bis-GMA and TEGDMA) network by DSC and 13C solution and solid-state NMR spectroscopy. Biomaterials. 2000;21:1897–903. https://doi.org/10.1016/S0142-9612(00)00067-3.
38. Sompalli NK, Mohan AM, Rao CVSB, Nagarajan S, Deivasigamani P. Tailor-made porous polymer and silica monolithic designs as probe anchoring templates for the solid-state naked eye sensing and preconcentration of hexavalent chromium. Sensors Actuators B Chem. 2019;298:126896. https://doi.org/10.1016/j.snb.2019.126896.
39. Madhesan T, Mohan AM. Porous silica and polymer monolith architectures as solid-state optical chemosensors for Hg^{2+} ions. Anal Bioanal Chem. 2020;412:7357–70. https://doi.org/10.1007/s00216-020-02870-8.
40. Sompalli NK, Deivasigamani P. Structurally designed porous polymer monoliths as probe anchoring templates as benign and fast responsive solid-state optical sensors for the sensing and recovery of copper ions. Nanotechnology. 2020;31:414004. https://doi.org/10.1088/1361-6528/ab9e2a.